

Forming an O Star via Disk Accretion?

Keping Qiu^{1,2}, Qizhou Zhang³, Henrik Beuther⁴, Cassandra Fallscheer^{4,5}

kqiu@mpifr-bonn.mpg.de

ABSTRACT

We present a study of outflow, infall, and rotation in a $\sim 10^5 L_\odot$ star-forming region, IRAS 18360-0537, with Submillimeter Array (SMA) and IRAM 30m observations. The 1.3 mm continuum map shows a 0.5 pc dust ridge, of which the central compact part has a mass of $\sim 80 M_\odot$ and harbors two condensations, MM1 and MM2. The CO (2–1) and SiO (5–4) maps reveal a biconical outflow centered at MM1, which is a hot molecular core (HMC) with a gas temperature of 320 ± 50 K and a mass of $\sim 13 M_\odot$. The outflow has a gas mass of $54 M_\odot$ and a dynamical timescale of 8×10^3 yr. The kinematics of the HMC is probed by high-excitation CH₃OH and CH₃CN lines, which are detected at sub-arcsecond resolution and unveil a velocity gradient perpendicular to the outflow axis, suggesting a disk-like rotation of the HMC. An infalling envelope around the HMC is evidenced by CN lines exhibiting a profound inverse P-Cygni profile, and the estimated mass infall rate, $1.5 \times 10^{-3} M_\odot \text{ yr}^{-1}$, is well comparable to that inferred from the mass outflow rate. A more detailed investigation of the kinematics of the dense gas around the HMC is obtained from the ¹³CO and C¹⁸O (2–1) lines; the position-velocity diagrams of the two lines are consistent with the model of a free-falling and Keplerian-like rotating envelope. The observations suggest that the protostar of a current mass $\sim 10 M_\odot$ embedded within MM1 will develop into an O star via disk accretion and envelope infall.

Subject headings: stars: formation — stars: early-type — ISM: kinematics and dynamics — ISM: jets and outflows

¹Max-Planck-Institut für Radioastronomie, Auf dem Hügel 69, 53121 Bonn, Germany

²Key Laboratory of Modern Astronomy and Astrophysics (Nanjing University), Ministry of Education, Nanjing 210093, China

³Harvard-Smithsonian Center for Astrophysics, 60 Garden Street, Cambridge, Massachusetts 02138, USA

⁴Max-Planck-Institut für Astronomie, Königstuhl 17, 69117 Heidelberg, Germany

⁵Department of Physics and Astronomy, University of Victoria, 3800 Finnerty Road, Victoria, BC V8P 5C2, Canada

1. Introduction

The formation process of high-mass stars ($> 8 M_{\odot}$) is poorly understood (Zinnecker & Yorke 2007). One key question in the field is whether high-mass stars form as a scaled-up version of low-mass star formation (e.g., Keto & Zhang 2010; Johnston et al. 2011). In a standard paradigm of low-mass star formation, a protostar accretes from a circumstellar disk embedded within an infalling envelope (Shu et al. 1987). Since accretion disks and collimated outflows are physically connected, the detection of well collimated outflows in an increasing number of high-mass star-forming regions supports an accretion-based scenario for massive star formation (e.g., Beuther et al. 2002; Zhang et al. 2007a; Zhang et al. 2007b; Qiu et al. 2007; Qiu & Zhang 2009; Qiu et al. 2011a; Zapata et al. 2011). In the meantime, great efforts have been made in searching for direct evidence for an infalling envelope and a rotating disk in association with massive star formation. Nevertheless, only a very few massive star-forming cores have been found to show clear signatures of both infall and rotation. Beltrán (2011) enlists a sample of six such sources from the literature, G10.62-0.38, G19.61-0.23, G24.78+0.08 A1, G31.41+0.31, W51 e2, and W51 North. But some more cases exist (e.g., NGC 7538 IRS 1, Qiu et al. 2011b; Beuther et al. 2012). In these studies, a rotation is inferred from a velocity gradient seen in high-density tracing molecular lines and an infall is probed by molecular lines with redshifted absorption against a bright continuum source. Even this small sample should be taken with caution. For example, the orientations of the velocity gradients may change by tens of degrees, depending on the lines being analyzed (e.g., W51 e2: Zhang & Ho 1997; Zhang et al. 1998; Keto & Klaassen 2008; Klaassen et al. 2009). Meanwhile, if a velocity gradient is arising from a rotating disk, it is expected to be perpendicular to a bipolar outflow, but for most sources in the sample, such an association between a putative disk and an outflow is yet to be confirmed (e.g., G31.41+0.31, Cesaroni et al. 2011, and references therein). Therefore, identifying and characterizing clear-cut examples showing self-consistent outflow, infall, and rotation motions remains of great interest to our understanding of massive star formation. Here we present such a study toward IRAS 18360-0537, using Submillimeter Array⁶ (SMA) $0.''5$ – $1.''5$ resolution observations in the 1.3 mm waveband.

IRAS 18360-0537 has a kinematic distance of 6.3 kpc and a far-IR luminosity of $1.2 \times 10^5 L_{\odot}$ (Molinari et al. 1996). In earlier single-dish surveys, the region was found to be associated with water maser emission (Palla et al. 1991; Brand et al. 1994) and thermal NH_3 (Molinari et al. 1996) and CS (Bronfman et al. 1996) emission. There is so far no report on high-angular-resolution observations of the region in (sub)millimeter or centimeter

⁶The SMA is joint project between the Smithsonian Astrophysical Observatory and the Academia Sinica Institute of Astronomy and Astrophysics and is funded by the Smithsonian Institution and the Academia Sinica.

wavelengths.

2. Observations

The SMA observations were undertaken in two frequency setups, each with two array configurations. The observing campaign was designed to cover CO, ^{13}CO , C^{18}O (2–1), and several CH_3OH and CH_3CN lines in one frequency setup and to cover CN ($N=2-1$) and SiO (5–4) lines in the other setup. The CO and SiO lines are typical outflow tracers, while the CN lines may reveal potential infall signatures in high-mass star-forming cores (Zapata et al. 2008; Wu et al. 2009). The kinematics of the innermost dense gas can be inferred from high-excitation CH_3OH and CH_3CN lines. The details of the observations are presented in Table 1.

The data were calibrated using the IDL MIR package, and imaged with the MIRIAD software. A continuum data set was constructed from line free channels using the MIRIAD task UVLIN. We performed self-calibration on the continuum, and applied the solutions to both continuum and line data sets. For molecular line maps within each frequency setup, the calibrated visibilities from the two array configurations were jointly imaged. The angular resolution (the synthesized beam, θ_{syn} , and its position angle, PA) and rms noise level, σ , of a map vary with the visibility weighting algorithm. Most maps were made with a compromise between resolution and sensitivity (e.g., varying the ROBUST parameter), resulting in $\theta_{\text{syn}} \sim 2.''7 \times 1.''4$ at $\text{PA} \sim 62^\circ$, $\sigma \sim 50 \text{ mJy beam}^{-1}$ per 1.5 km s^{-1} in CO lines, $\theta_{\text{syn}} \sim 2.''0 \times 1.''4$ at $\text{PA} \sim 64^\circ$, $\sigma \sim 30 \text{ mJy beam}^{-1}$ per 1.5 km s^{-1} in SiO (5–4), and $\theta_{\text{syn}} \sim 1.''4 \times 1.''3$ at $\text{PA} \sim 57^\circ$, $\sigma \sim 35 \text{ mJy beam}^{-1}$ per 0.6 km s^{-1} in CN lines. To achieve the highest possible angular resolution, which is desirable in searching for disk-like structures, the CH_3OH and CH_3CN lines were made with a uniform weighting, leading to $\theta_{\text{syn}} \sim 0.''8 \times 0.''6$ at $\text{PA} \sim 20^\circ$, $\sigma \sim 65 \text{ mJy beam}^{-1}$ per 0.6 km s^{-1} . For the 1.3 mm continuum emission, we made a map combining visibilities from all four array configurations (Figure 1(a)), with $\theta_{\text{syn}} \sim 1.''6 \times 1.''2$ at $\text{PA} \sim 68^\circ$, $\sigma \sim 1.5 \text{ mJy beam}^{-1}$, and a map combining the EXT and VEX data (Figure 1(b)), with $\theta_{\text{syn}} \sim 0.''6 \times 0.''5$ at $\text{PA} \sim 18^\circ$, and $\sigma \sim 2.7 \text{ mJy beam}^{-1}$.

The IRAM⁷ 30m telescope was used to fill the zero-spacing of the SMA maps in CO and ^{13}CO (2–1). The observations were conducted on 2007 November 1. A $2' \times 2'$ region centered at (R.A., Dec.)_{J2000}=(18^h38^m40^s.3, –5°35'6.''0) was mapped in the on-the-fly mode. Scans were made in both Right Ascension and Declination directions in an effort to prevent systematic scanning effects from appearing in the data. The receiver was tuned to 230.538

⁷IRAM is supported by INSU/CNRS (France), MPG (Germany) and IGN (Spain).

GHz and 220.399 GHz for the CO and ^{13}CO (2–1) lines, respectively, and the spectra have a 0.4 km s^{-1} resolution. The spectra were processed using CLASS in the GILDAS software package. The CO spectra have an rms noise level of 1.1 K and the ^{13}CO spectra have an rms of 0.5 K in T_{mb} . The combination of the SMA and single-dish data was performed in MIRIAD following a procedure outlined in Zhang et al. (1995).

3. Results

3.1. Dust Condensations

Figure 1(a) shows the 1.3 mm continuum map made from observations conducted with the four array configurations. The emission reveals a northwest-southeast (NW-SE) ridge with a bright and compact part at the center. In Figure 1(b), relatively extended emission is filtered out in the map made with the EXT and VEX data, and the central part is resolved into two condensations, MM1 and MM2. This work focuses on the brightest dust condensation, MM1. It shows very faint free-free emission ($\sim 0.5 \text{ mJy}$ at 1–3 cm) in our Very Large Array observations (Qiu et al. in prep.). The observed 1.3 mm continuum emission is completely dominated by dust emission.

MM1 shows rich emission lines in complex organic molecules, e.g., CH_3OH , CH_3CN , $\text{C}_2\text{H}_3\text{CN}$, and $\text{C}_2\text{H}_5\text{CN}$. The CH_3CN (12–11) K -ladder is a good thermometer of dense gas in high-mass star-forming regions. Following Qiu & Zhang (2009) and Qiu et al. (2011b), we simultaneously fit the $K = 2$ –8 components⁸, taking into account the optical depth effect. The systemic velocity, 103.5 km s^{-1} , is determined from Gaussian fittings to the $K = 7, 8$ components, which are of the highest excitation and not heavily blended with other lines. This determination is concurred by the $\text{C}_2\text{H}_5\text{CN}$ ($25_{22,4}$ – $24_{22,3}$) and $\text{CH}_3^{13}\text{CN}$ (12_2 – 11_2) lines (see Figure 2), to which Gaussian fittings give velocities of 102.9 and 103.5 km s^{-1} , respectively. In Figure 2, the best-fit model reasonably matches the observation, and yields a gas temperature of $320 \pm 50 \text{ K}$, where the uncertainty accounts for the 1σ noise level. The fitting assumes that all the K components are tracing the same gas under local thermodynamic equilibrium conditions. Provided potential density and temperature gradients for an internally heated protostellar core, the best-fit model may represent a characteristic estimate.

Assuming thermal equilibrium between the dust and dense gas, the derived gas temperature in MM1 approximates the dust temperature. To constrain the dust opacity index, β , we make use of the $880 \mu\text{m}$ continuum data obtained from recent SMA observations.

⁸The relatively low excitation $K = 0, 1$ components are resolved out in the VEX data.

By comparing the 1.3 mm and 880 μm continuum maps constructed with the same (u, v) range, we deduce $\beta = 0.82$ toward MM1 and $\beta = 0.50$ toward MM2, corresponding to dust opacities of 2.5 and 4.3 $\text{cm}^2 \text{g}^{-1}$, respectively, at 1.3 mm (Hildebrand 1983). The gas mass of MM1 is then estimated from its 1.3 mm dust continuum flux, 0.76 Jy, to be $13 M_{\odot}$, by adopting a canonical gas-to-dust mass ratio of 100. The mass of MM2 is less clear given its unknown gas or dust temperature. Adopting a temperature of 30 K deduced from prior NH_3 observations (Molinari et al. 1996), one obtains a mass of $25 M_{\odot}$ from the continuum flux of 0.2 Jy.

3.2. Bipolar Outflow

Figure 3 shows the velocity integrated CO (2–1) and SiO (5–4) emission observed with the SMA. Both CO and SiO emission seems to be dominated by a northeast-southwest (NE-SW) bipolar outflow centered at MM1. The outflow has a biconical shape with an opening angle of $\sim 65^\circ$. Such an outflow is often thought to form from ambient gas being swept up or entrained by a wide-angle wind (e.g., Shepherd et al. 1998; Qiu et al. 2009). A blueshifted clump to the south of MM1 and a redshifted clump to the north, which are more prominent in the CO map, could be part of the biconical outflow, if the wide-angle wind is slightly inclined to the plane of sky and impinges into an environment with an inhomogeneous density structure. However, the possibility that the two clumps form another outflow cannot be ruled out.

Figure 4 shows the velocity channel maps of the CO emission observed with the SMA; at low velocities (96–112.5 km s^{-1}), the maps made with the combined SMA and IRAM 30m (SMA+30m) data are also presented. It is clear that the combined data effectively recover extended emission around the cloud velocity. Emission arising from outflow structures appears predominant in channels of $\leq 100.5 \text{ km s}^{-1}$ and $\geq 106.5 \text{ km s}^{-1}$. In particular, the cone-shaped structure of the SW lobe is most noticeable in the 106.5 km s^{-1} channel map. The emission at 111.0 and 112.5 km s^{-1} is mostly filtered out in the SMA maps and appears to be dominated by diffuse gas in the combined maps. This is most likely due to the self-absorption effect caused by a foreground cloud. Figure 5 shows the SiO (5–4) channel maps. SiO is believed to be produced in the gas phase through shock-driven sputtering of Si-bearing species on dust grains (Schilke et al. 1997). Therefore the SiO emission is not contaminated by emission from quiescent ambient gas. As seen in the integrated map, the SiO outflow is in general consistent with the outflow seen in the CO emission.

Figure 6 shows the SMA ^{13}CO (2–1) channel maps as well as the SMA+30m maps at low velocities. The ^{13}CO emission arising from the NE-SW outflow is less extended than

that in CO (2–1), but is still appreciable in the channels of 94.5–108.0 km s^{−1} (except the 103.5 km s^{−1} channel). In the close vicinity of MM1, the ¹³CO emission peaks to the NW of MM1 at blueshifted velocities and to the SE at redshifted velocities; the offset between the ¹³CO peak and dust continuum peak decreases with the velocity so that the ¹³CO emission approximately coincides with MM1 at the highest velocities. On the other hand, the CO (2–1) emission peak is clearly offset from MM1 even at the highest velocities, and shifts from the NE to SW. Such a difference is highlighted in Figure 7. While the relatively extended emission in ¹³CO traces the outflow, the compact and bright emission closely around MM1 is predominantly arising from a dense envelope.

3.3. Velocity Gradients in High-excitation CH₃OH and CH₃CN Lines

The ¹³CO (2–1) observations provide hints for the rotation of dense gas around MM1 (Figure 7). However, the ¹³CO (2–1) line is affected by the outflow and, with a critical density, n_{cr} , of order 10⁴ cm^{−3} and an upper level energy, E_{up} , around 16 K above the ground, cannot effectively probe the hot and dense gas within MM1. To search for a potential disk-like structure, which is supposed to lie in the innermost part of a molecular core, we inspected high-excitation lines from less abundant molecular species. A NW-SE velocity gradient across MM1 is consistently seen. Figure 8 shows the zeroth moment (velocity integrated emission) and first moment (intensity weighted velocity) maps, and position-velocity (P - V) diagrams of the CH₃OH (15_{4,11}–16_{3,13}) E , CH₃CN (12₇–11₇), and vibrational CH₃CN (12₁–11₁) lines. These lines are chosen for the following reasons. First, they are highly excited ($E_{\text{up}} > 350$ K) and, as evidenced by the zeroth moment maps, probe the innermost dense gas in MM1. Second, they are not significantly blended with other lines; CH₃CN (12₇–11₇) is slightly blended with CH₃¹³CN (12₅–11₅), but the two lines are ~ 9.5 km s^{−1} apart and the former is three times brighter than the latter, so it is feasible to ignore the contribution from CH₃¹³CN (12₅–11₅) in interpreting CH₃CN (12₇–11₇). Finally, these lines are detected with sufficient signal-to-noise ratios in the VEX observations so that the velocity gradient is discernable at a 0".4 resolution; some other lines with a higher E_{up} , e.g., CH₃CN (12₈–11₈), or with a lower optical depth, e.g., CH₃¹³CN (12₂–11₂), are subject to limited signal-to-noise ratios and barely show the NW-SE velocity gradient. From the first moment maps of CH₃OH (15_{4,11}–16_{3,13}) E and CH₃CN (12₇–11₇), the velocity gradient is approximately along a position angle (PA) of 140°, which is adopted for the cut of the P - V diagrams. The vibrational CH₃CN (12₁–11₁) line has the highest excitation and lowest signal-to-noise ratio among the three lines shown here. The direction of the velocity gradient in its first-moment map is less clear, but an overall NW-SE gradient is still discernable and the P - V pattern is consistent with those of the other two lines. Compared to the orientation of the biconical NE-SW outflow, the

CH₃OH and CH₃CN velocity gradient is approximately perpendicular to the outflow axis, and is apparently arising from a disk-like rotation. However, neither the dust continuum nor the molecular line maps of the MM1 condensation shows a flattened morphology. This is very likely due to insufficient angular resolutions ($\gtrsim 0''.5$) of the observations.

3.4. Infall Signatures Seen in CN ($N=2-1$)

Several CN ($N=2-1$) hyperfine lines are detected toward MM1. The brightest three, i.e., the $J=5/2-3/2$, $F=5/2-3/2$ ($\nu_0=226.87417$ GHz), $J=5/2-3/2$, $F=7/2-5/2$ (226.87474 GHz), and $J=5/2-3/2$, $F=3/2-1/2$ (226.87590 GHz) lines, are heavily blended and form a triplet. Besides the triplet, the lines of $J=3/2-1/2$, $F=5/2-3/2$ (226.65956 GHz) and $J=3/2-1/2$, $F=3/2-1/2$ (226.67931 GHz) are detected as well; these two lines do not suffer from line blending and the brighter one, CN ($N=2-1$, $J=3/2-1/2$, $F=5/2-3/2$), is shown in Figure 9. The CN ($N=2-1$) transitions have $E_{\text{up}} \sim 16$ K and n_{cr} of order 10^7 cm⁻³, probing relatively cold gas in a dense envelope around MM1. All the detected CN lines show emission at blueshifted velocities and absorption at redshifted velocities, i.e., an inverse P-Cygni profile. Such a profile is often interpreted to indicate an infall of matter, whereas the absorption mostly comes from the gas on the near side of a central source and the emission is attributed to the gas in the far side (e.g., Zapata et al. 2008; Wu et al. 2009; Qiu et al. 2011b). Therefore, the CN lines probe an infalling envelope around MM1. In Figure 9, the peaking velocities of the emission and absorption are slightly asymmetric with respect to the systemic velocity. It could be in part due to the uncertainty in determining the systemic velocity, which is estimated to be 103.5 km s⁻¹ in our data but was suggested to be 102.3 km s⁻¹ based on single-dish NH₃ observations (Molinari et al. 1996).

4. Discussion

4.1. An accreting star of $\sim 10 M_{\odot}$

MM1 has a gas temperature of 320 K and molecular chemistry characteristic of a hot molecular core (HMC). At least one high-mass protostar has formed in MM1. On the other hand, only very faint and spatially unresolved radio continuum emission is detected. The emission can be arising from an ionized jet or wind, or from a hypercompact H II region. In the latter case, the central ionizing star has an equivalent spectral type of B0.5, corresponding to a stellar mass, M_* , of $12 M_{\odot}$ (Schaller et al. 1992). The mass of the outflowing gas can also shed light on the stellar mass of the protostar. Assuming that the molecular outflow

is momentum driven by an underlying wind, the accumulated mass ejected to the wind is $M_{\text{out}}v_{\text{out}}/v_w$, where M_{out} is the outflow mass, v_{out} the outflow velocity, and v_w the wind speed. The mass loss rate to the wind is a fraction, f , of the mass infall rate, thus the mass of the forming star can be expressed as $M_{\text{out}}v_{\text{out}}/v_w \cdot (1 - f)/f$ (see also Lada & Fich 1996). The outflow mass is calculated from the CO line wings ($\leq 100.5 \text{ km s}^{-1}$ and $\geq 106.5 \text{ km s}^{-1}$), assuming an excitation temperature of 30 K and a CO abundance of 10^{-4} . To correct for the optical depth effect, we compare the CO and ^{13}CO (2–1) fluxes and adopt a C-to- ^{13}C abundance ratio of 37 (Wilson & Rood 1994). A more detailed description of the calculation procedure can be found in Qiu et al. (2009). We derive an outflow mass of $54 M_{\odot}$ with the combined SMA and IRAM 30m data. The maximum velocity of the outflow observed in CO (2–1) is about 36 km s^{-1} . Adopting a wind speed of 500 km s^{-1} (e.g., Martí et al. 1998) and $f = 1/3$ (Tomisaka 1998; Shu et al. 2000), the accumulated stellar mass is about $8 M_{\odot}$, in agreement with the above estimate.

The stellar luminosity of a $\sim 10 M_{\odot}$ star at the Zero-Age-Main-Sequence (ZAMS) is $\sim 10^4 L_{\odot}$, only a small fraction of the total luminosity observed in IRAS 18360-0537 ($\sim 10^5 L_{\odot}$). The majority of the observed luminosity presumably comes from accretion shocks. The accretion luminosity can be estimated from $GM_*\dot{M}/R_*$, where \dot{M} is the mass flux of the accretion onto the star and R_* the radius of the star. Again, under the assumption of momentum conservation between the molecular outflow and the underlying wind, \dot{M} can be inferred from the mass outflow rate. Without correcting for an unknown inclination angle, the dynamical timescale of the outflow, i.e., a half of the outflow extension ($\sim 0.3 \text{ pc}$) divided by the terminal velocity, is about $8 \times 10^3 \text{ yr}$. The mass outflow rate is then $7 \times 10^{-3} M_{\odot} \text{ yr}^{-1}$, leading to a mass infall rate of $1.5 \times 10^{-3} M_{\odot} \text{ yr}^{-1}$ and $\dot{M} \sim 1.0 \times 10^{-3} M_{\odot} \text{ yr}^{-1}$. If we adopt a radius of $4R_{\odot}$ for a $10 M_{\odot}$ star at the ZAMS (Panagia 1973; Schaller et al. 1992), the accretion luminosity amounts to $8 \times 10^4 L_{\odot}$, which does appear to dominate the total luminosity.

Alternatively, according to the model of Hosokawa et al. (2010), massive protostars with disk accretion rates of $10^{-3} M_{\odot} \text{ yr}^{-1}$ attain a total luminosity of $\sim 10^5 L_{\odot}$ as M_* increases to $\sim 15 M_{\odot}$, and reach the ZAMS for $M_* \simeq 30 M_{\odot}$. In this model, the stellar radius swells to tens of R_{\odot} as M_* reaches $\sim 10 M_{\odot}$, so the accretion luminosity is only of order $10^4 L_{\odot}$, while the stellar radiation, which comes from the release of the gravitational energy, is dominating the total luminosity. The large radius of the protostar also reduces the effective temperature and the UV luminosity, thus the faint radio continuum emission is expected to be arising from an ionized jet or wind.

Nevertheless, the protostar embedded in MM1 appears to have a current mass of $\sim 10 M_{\odot}$ and is in an active accretion phase.

4.2. Rotation and Infall

Is the accretion onto the central high-mass protostar mediated by a rotating disk? The observed CO and SiO outflow supports a positive answer since a biconical outflow is expected to originate from an accretion disk in low-mass star formation (see Qiu et al. 2009, for a detailed comparison between wide-angle outflows in low-mass and high-mass star formation). The high-excitation CH₃OH and CH₃CN lines observed at sub-arcsecond resolution provide direct evidence for the rotation of the HMC. There seem to be hints of a Keplerian-like motion in the P - V diagrams of the high-excitation lines. For example, in the upper right quadrant of Figure 8(e), the maximum velocity increases with the decreasing offset; in the lower left quadrant of Figure 8(d), a secondary peak around 98.5 km s⁻¹ could be attributed to a Keplerian-like motion as well.

A more detailed investigation of the rotation curve of the HMC awaits future observations with greatly improved resolution and sensitivity. Here we look into the lines from more abundant molecular species, i.e., C¹⁸O and ¹³CO, which may help to deliver a more complete view of the velocity field for the dense gas on a larger scale (e.g., Cesaroni et al. 2011). ¹³CO (2–1) can be contaminated by the outflow, but from Figure 7, the emission in the close vicinity of MM1 is dominated by the dense envelope. In Figure 10(a) we plot the ¹³CO and C¹⁸O P - V diagrams, cut along the PA of 140°. We note that the ¹³CO and C¹⁸O emission arises from a region encompassing both MM1 and MM2. However, from the P - V diagrams the velocity field cannot be ascribed to an orbiting motion of a binary. In particular, the high-excitation lines shown in Figure 8 are not detected toward MM2; these lines show a clear velocity gradient across MM1. In Figure 10, the CH₃CN, C¹⁸O, and ¹³CO emission seems to be arising from different layers of a coherent structure centered at MM1, whereas MM2 is likely a fragment of this structure. Despite the missing flux closely around the cloud velocity, the ¹³CO P - V diagram shows a concave outer edge and is slightly skewed in a sense consistent with the velocity gradient seen in CH₃OH and CH₃CN. A similar pattern is discernible in the C¹⁸O P - V diagram, though the emission has a lower velocity dispersion and a smaller spatial extent compared to the ¹³CO emission. Such a P - V pattern may characterize a combination of infall and rotation (Cesaroni et al. 2011; Tobin et al. 2012). To corroborate this interpretation, we overlay in Figure 10 a free-fall and Keplerian-like rotation model which is described by Cesaroni et al. (2011). Since the C¹⁸O and ¹³CO emission mostly traces outer layers around the HMC, we set a central dynamical mass of 25 M_{\odot} , which is approximately the combined mass of the HMC and the embedded high-mass protostar, and an inner truncation radius of 0.''25 (0.008 pc), which is approximately the deconvolved radius of the CH₃OH and CH₃CN emission; the outer radius is set to be 3.''5 (0.1 pc), roughly the radius of the C¹⁸O and ¹³CO emission. The constructed model (solid curve) reasonably fits the C¹⁸O and ¹³CO P - V diagrams except the high velocity tail close to the zero offset seen

in ^{13}CO . That high velocity tail can be partly ascribed to the inner rotating and infalling gas, as illustrated by a scaled-down model (dashed curve in Figure 10) with a central mass of $10 M_{\odot}$ and outer and inner radii of $0.''25$ and $0.''032$ (200 AU), respectively, but it can also be arising from the outflowing gas. Overall the bulk ^{13}CO and C^{18}O emission delineates an infalling and rotating envelope around the HMC.

To assess the envelope mass, we performed a two-component Gaussian fitting to the central compact part of the dust ridge with the MIRIAD task IMFIT, and derived a flux 0.96 Jy for the component encompassing MM1. Subtracting the HMC contribution (0.76 Jy, see Section 3.1), the dust continuum flux from the cool envelope amounts to 0.2 Jy, resulting in a gas mass of $42 M_{\odot}$ for $\beta = 0.82$ and an adopted temperature of 30 K (Molinari et al. 1996). From the fitting, the MM2 component has a flux of 0.2 Jy, consistent with the measurement based on Figure 1(b) (Section 3.1). Hence, the total mass of the central compact part of the dust ridge reaches $80 M_{\odot}$, whereas the mass of the envelope traced by the ^{13}CO and C^{18}O emission amounts to $67 M_{\odot}$. Such a massive envelope is presumably gravitationally unstable. Indeed, MM2 is likely the consequence of the fragmentation of the envelope. However, the HMC itself has a gas mass ($13 M_{\odot}$) comparable to the mass of the accreting protostar ($10 M_{\odot}$), thus the latter can have an appreciable stabilizing effect on the former. Cesaroni et al. (2007) suggest that a rotational structure of a mass comparable to that of the central protostar, which is in turn less than $20 M_{\odot}$, resembles an accretion disk rather than a transient toroid. In this sense, we may expect that as the central protostar continues to accrete and increase its mass, the rotating HMC serves as an accretion disk, and finally dissipates by enhanced UV radiation (e.g., by photoevaporation, Hollenbach et al. 1994) rather than by gravitational fragmentation.

The infall motion of the envelope around the HMC is not only appreciable in the C^{18}O and ^{13}CO P - V diagrams, but also more unambiguously evidenced by the CN hyperfine lines with a profound inverse P-Cygni profile. The mass infall rate can be estimated from $4\pi r^2 \rho V_{\text{in}}$, where the infall velocity V_{in} is about 1.5 km s^{-1} according to the CN ($N=2-1$) profiles (e.g., Figure 9), r the radius of the envelope, and ρ the mass density. Considering that the CN lines were imaged with a synthesized beam ($1.''4 \times 1.''3$) similar to that of the dust continuum map in Figure 1(a) ($1.''6 \times 1.''2$), we estimate the radius and density based on the above two-component Gaussian fitting. For the component encompassing MM1, $r \simeq 0.''9$ (5700 AU) from the fitting, and the averaged number density is $8 \times 10^6 \text{ cm}^{-3}$ for a gas mass of $42 M_{\odot}$. The mass infall rate is then found to be about $1.5 \times 10^{-3} M_{\odot} \text{ yr}^{-1}$. From the model shown in Figure 10, the free-fall velocity reaches 3 km s^{-1} at $r \sim 0.''9$, a factor of two higher than inferred from the CN profiles. Such a discrepancy can be ascribed to the deviation of the infall motion from the modeled free-fall, the uncertainty of the systemic velocity (see Section 3.4), or an underestimate of the radius from the two-component fitting. Nevertheless, since

the (free-fall plus Keplerian-like rotation) model parameters are not stringently constrained and the CN profiles provide an averaged estimate, the discrepancy is not significant. On the other hand, as discussed above, the mass outflow rate implies a mass infall rate of $1.5 \times 10^{-3} M_{\odot} \text{yr}^{-1}$. Though both are subject to large uncertainties, the two independent estimates of the mass infall rate appear to agree with each other, suggesting that the envelope infall is feeding the accretion onto one protostar, i.e., the $\sim 10 M_{\odot}$ star embedded in MM1. Provided its high accretion rate and the massive gas reservoir available from the envelope, it is reasonable to expect that the star would significantly increase its mass and develop into an O star.

5. Summary

We have presented high-angular-resolution dust continuum and molecular line observations toward IRAS 18360-0537, a $\sim 10^5 L_{\odot}$ star-forming region. The region shows a 0.5 pc dust ridge, harboring two massive condensations, MM1 and MM2, in the central part. MM1, a HMC with a gas temperature of 320 K and a mass of $13 M_{\odot}$, is embedded within an infalling envelope, and appears to be rotating about the axis of a bipolar outflow.

The outflow is seen in CO (2–1) and SiO (5–4) and shows a biconical shape centered at MM1. The gas mass of the outflow is estimated to be $54 M_{\odot}$, and the dynamical timescale is 8×10^3 yr. The rotation of the HMC is inferred from sub-arcsecond observations of high-excitation CH₃OH and CH₃CN lines, which show a velocity gradient approximately perpendicular to the outflow axis. On the other hand, the infall motion of the envelope around the HMC is probed by CN ($N=2-1$) hyperfine lines, which exhibit a profound inverse P-Cygni profile. The estimated mass infall rate is $1.5 \times 10^{-3} M_{\odot} \text{yr}^{-1}$, comparable to that inferred from the mass outflow rate. Further information on the kinematics of the gas around the HMC is obtained from the C¹⁸O and ¹³CO (2–1) lines, whose P - V diagrams can be described with a model of a free-falling and Keplerian-like rotating envelope. With these observations, we speculate that a protostar in MM1, which we suggest to have a current mass of $\sim 10 M_{\odot}$, will grow into an O star via disk accretion and envelope infall, i.e., through a process similar to the standard paradigm for low-mass star formation.

REFERENCES

- Beltrán, M. T. 2011, Computational Star Formation, Proceedings of the International Astronomical Union, IAU Symposium, 270, 33

- Beuther, H., Linz, H., & Henning, T. 2012, arXiv: 1205.5459
- Beuther, H., Schilke, P., Gueth, F., McCaughrean, M., Andersen, M., Sridharan, T. K., & Menten, K. M. 2002, *A&A*, 387, 931
- Brand, J. et al. 1994, *A&AS*, 103, 541
- Bronfman, L., Nyman, L.-Å., & May, J. 1996, *A&AS*, 115, 81
- Cesaroni, R., Beltrán, M., Zhang, Q., Beuther, H., & Fallscheer, C. 2011, *A&A*, 533, 73
- Cesaroni, R., Galli, D., Lodato, D., Walmsley, C. M., & Zhang, Q. 2007, *Protostars and Planets V*, ed. B. Reipurth et al. (Tucson, AZ: Univ. Arizona Press), 951
- Hildebrand, R. H. 1983, *QJRAS*, 24, 267
- Hollenbach, D., Johnstone, D., Lizano, S., & Shu, F. H. 1994, *ApJ*, 428, 654
- Hosokawa, T., Yorke, H. W., & Omukai, K. 2010, *ApJ*, 721, 478
- Keto, E. & Klaassen, P. 2008, *ApJ*, 678, L109
- Keto, E. & Zhang, Q. 2010, *MNRAS*, 406, 102
- Johnston, K. G., Keto, E., Robitaille, T. P., & Wood, K. 2011, *MNRAS*, 415, 2953
- Klaassen, P., D., Wilson, C., D., Keto, E. R., & Zhang, Q. 2009, *ApJ*, 703, 1308
- Lada, C. J. & Fich, M. 1996, *ApJ*, 459, 638
- Martí, J., Rodríguez, L. F., & Reipurth, B. 1998, *ApJ*, 502, 337
- Molinari, S., Brand, J., Cesaroni, R., & Palla, F. 1996, *A&A*, 308, 573
- Palla, F., Brand, J., Cesaroni, R., Comoretto, G., & Felli, M. 1991, *A&A*, 246, 249
- Panagia, N. 1973, *AJ*, 78, 929
- Schilke, P., Walmsley, C. M., Pineau des Forêts, G., & Flower, D. R. 1997, *A&A*, 321, 293
- Qiu, K. & Zhang, Q. 2009, *ApJ*, 702, L66
- Qiu, K., Zhang, Q., Beuther, H., & Yang, J. 2007, *ApJ*, 654, 361
- Qiu, K., Zhang, Q., Wu, J., & Chen, H.-R. 2009, *ApJ*, 696, 66

- Qiu, K., Wyrowski, F., Menten, K. M., Güsten, R., Leurini, S., & Leinz, C. 2011, *ApJ*, 743, L25
- Qiu, K., Zhang, Q., & Menten, K. M. 2011, *ApJ*, 728, 6
- Schaller, G., Schaerer, D., Meynet, G., & Maeder, A. 1992, *A&AS*, 96, 269
- Shepherd, D. S., Watson, A. M., Sargent, A. I., & Churchwell, E. 1998, *ApJ*, 507, 861
- Shu, F. H., Adams, F. C., & Lizano, S. 1987, *ARA&A*, 25, 23
- Shu, F. H., Najita, J. R., Shang, H., & Li, Z.-Y. 2000, *Protostars and Planets IV*, ed. V. Mannings et al. (Tucson, AZ: Univ. Arizona Press), 789
- Tobin, J. J. et al. 2012, *ApJ*, 748, 16
- Tomisaka, K. 1998, *ApJ*, 502, L163
- Wilson, T. L. & Rood, R. 1994, *ARA&A*, 32, 191
- Wu, Y. et al. 2009, *ApJ*, 697, L116
- Zapata, L. A., Rodríguez-Garza, C., Rodríguez, L. F., Girart, J. M., & Chen, H.-R. 2011, *ApJ*, 740, L19
- Zapata, L. A., Palau, A., Ho, P. T. P., Schilke, P., Garrod, R. T., Rodríguez, L. F., & Menten, K. 2008, *A&A*, 479, L25
- Zhang, Q. & Ho, P. T. P. 1997, *ApJ*, 488, 241
- Zhang, Q., Ho, P. T. P., & Ohashi, N. 1998, *ApJ*, 494, 636
- Zhang, Q., Ho, P. T. P., Wright, M. C., & Wilner, D. J. 1995, *ApJ*, 451, L71
- Zhang, Q., Hunter, T. R., Beuther, H., Sridharan, T. K., Liu, S.-Y., Su, Y.-N., Chen, H.-R., & Chen, Y. 2007a, *ApJ*, 658, 1152
- Zhang, Q., Sridharan, T. K., Hunter, T. R., Chen, Y., Beuther, H., & Wyrowski, F. 2007b, *A&A*, 470, 269
- Zinnecker, H. & Yorke, H. W. 2007, *ARA&A*, 45, 481

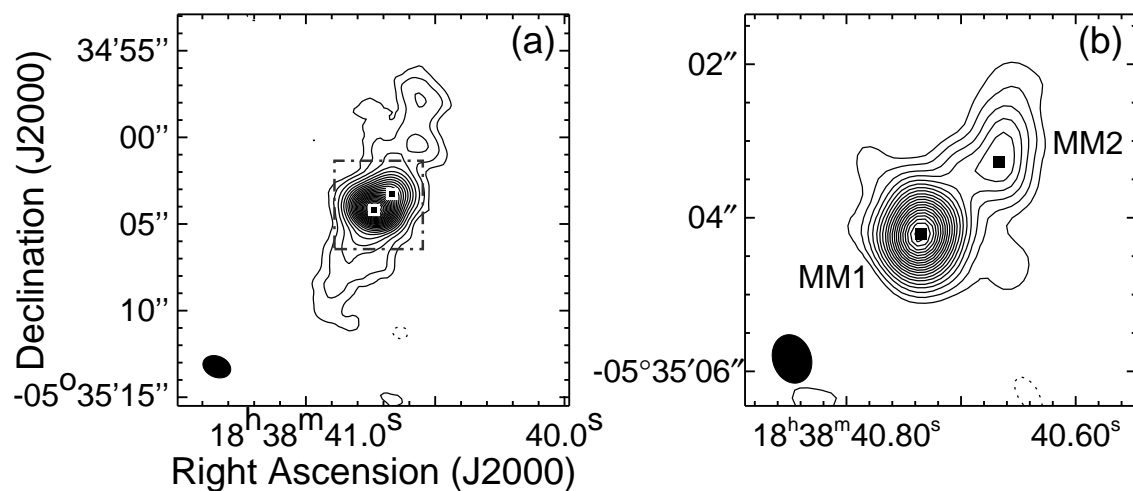


Fig. 1.— (a) 1.3 mm continuum map constructed by combining data from all the observations. Solid and dotted contours show positive and negative emission, respectively, with the contour levels of $6 \times (1, 2, 3, \dots, 23)^{1.5} \text{ mJy beam}^{-1}$. (b) Same as (a), but for the EXT and VEX data, and contour levels of $9 \times (1, 2, 3, \dots, 21)^{1.3} \text{ mJy beam}^{-1}$. In each panel (and hereafter), two filled squares denote the peak positions of the two condensations (MM1 and MM2), and a filled ellipse in the lower left shows the synthesized beam.

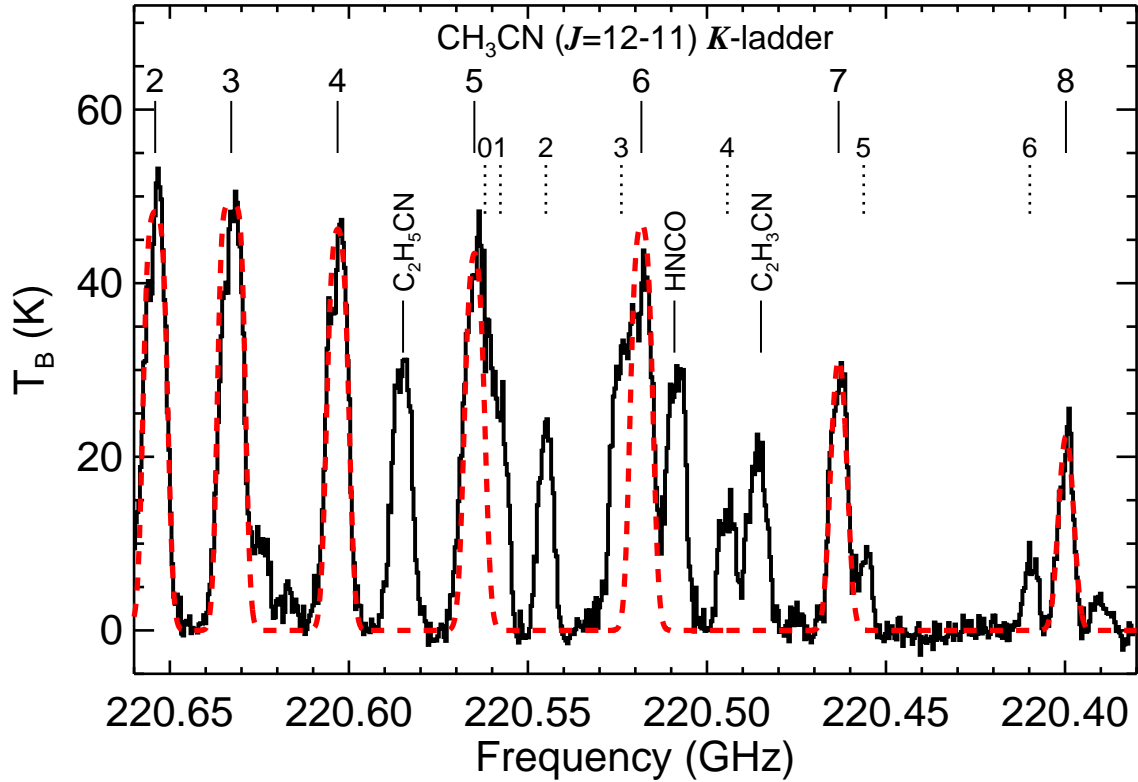


Fig. 2.— The spectra toward MM1, covering the $K=2-8$ ladder of CH₃CN (12–11), with the observations shown in black histograms and the best fit LTE model in dashed lines. The CH₃CN (12–11) $K=2-8$ components are labeled with solid bars, and the CH₃¹³CN (12–11) $K=0-6$ components with dotted bars. Some other lines covered in the frequency range are also denoted.

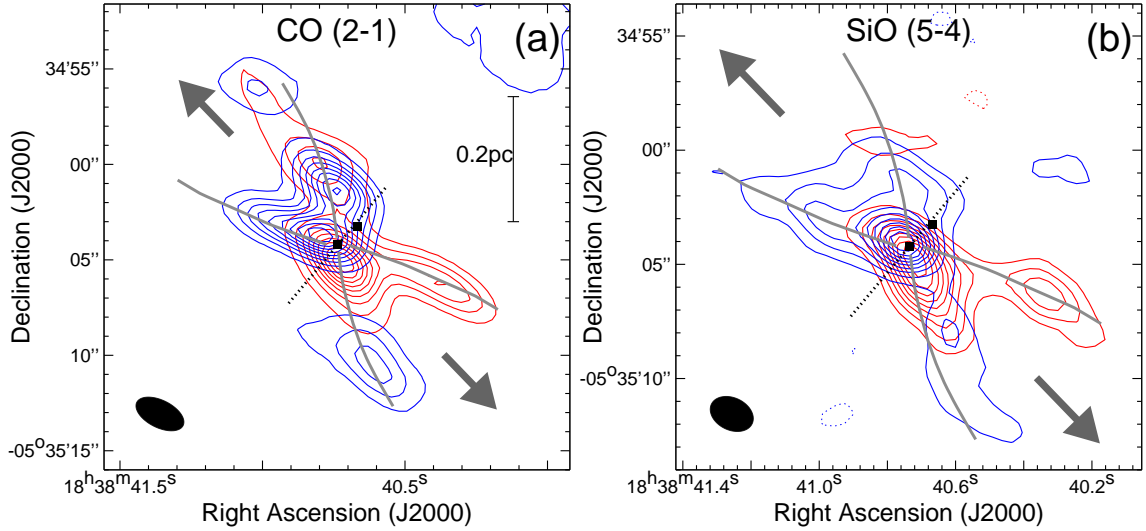


Fig. 3.— (a) CO (2–1) emission observed with the SMA, and integrated from 69 to 99 km s^{-1} for the blueshifted lobe and from 106.5 to 139.5 km s^{-1} for the redshifted lobe, shown in blue and red contours, respectively. The starting and spacing contour levels are 10% of the peak emission, which is 56.4 $\text{Jy beam}^{-1} \text{ km s}^{-1}$ for the blueshifted lobe and 71.3 $\text{Jy beam}^{-1} \text{ km s}^{-1}$ for the redshifted lobe. The gray curves outline a biconical outflow, and the two arrows indicate the orientation of the outflow axis. A dotted line marks the direction of a velocity gradient seen in MM1 (see Figure 8). (b) The same as (a), but for SiO (5–4). The blueshifted lobe is integrated from 88.5 to 102 km s^{-1} , and the redshifted lobe from 105 to 118.5 km s^{-1} . The starting and spacing contour levels are 10% of the peak emission, which is 6.7 $\text{Jy beam}^{-1} \text{ km s}^{-1}$ for the blueshifted lobe and 7.3 $\text{Jy beam}^{-1} \text{ km s}^{-1}$ for the redshifted lobe.

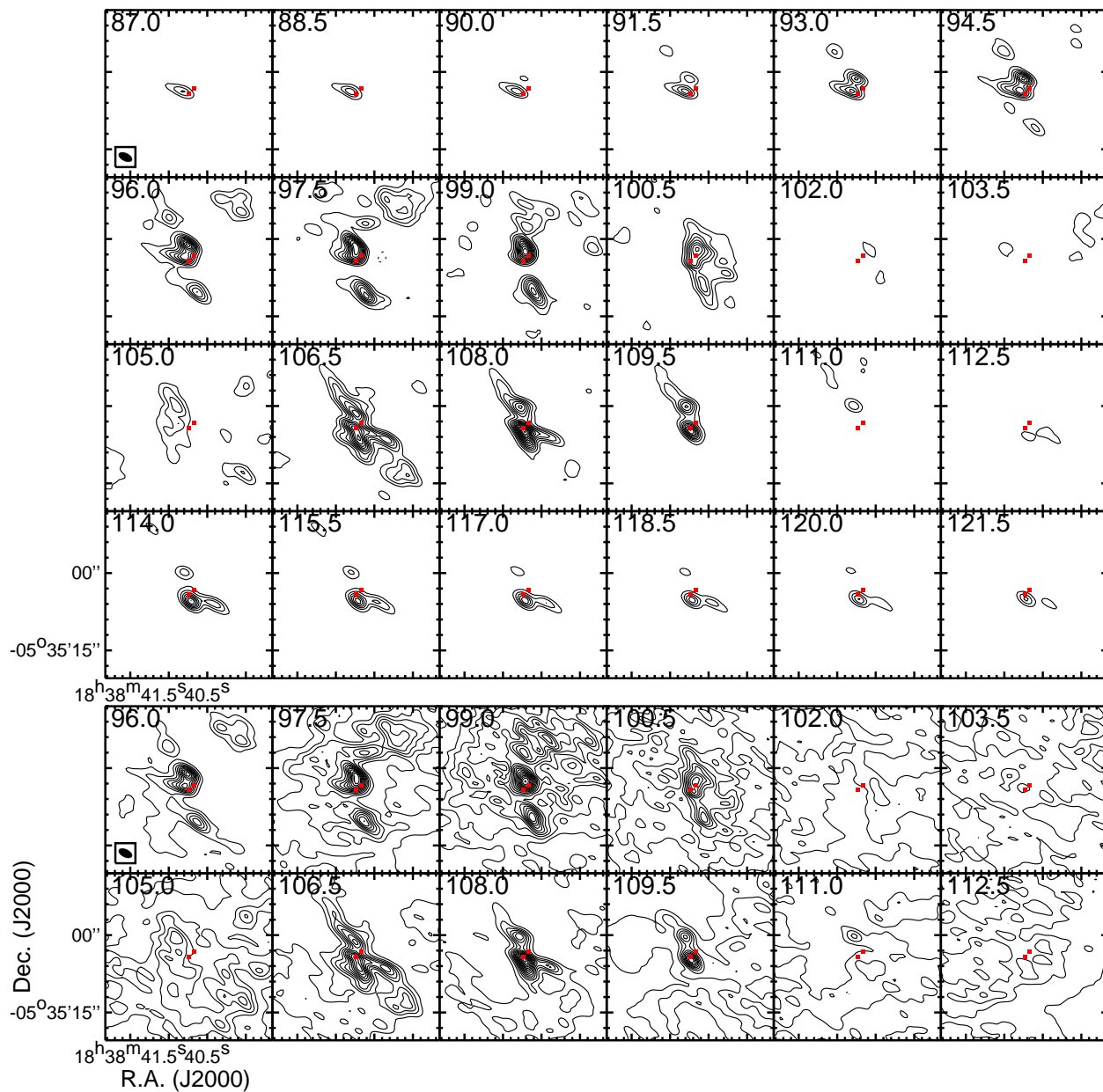


Fig. 4.— SMA CO (2–1) velocity channel maps. For channels of 96–112.5 km^s⁻¹, the maps made with the combined SMA and IRAM 30m data are shown on the bottom. Solid and dotted contours show the positive and negative emission, respectively, with the same absolute levels starting from and increasing in steps of 0.6 Jy beam⁻¹.

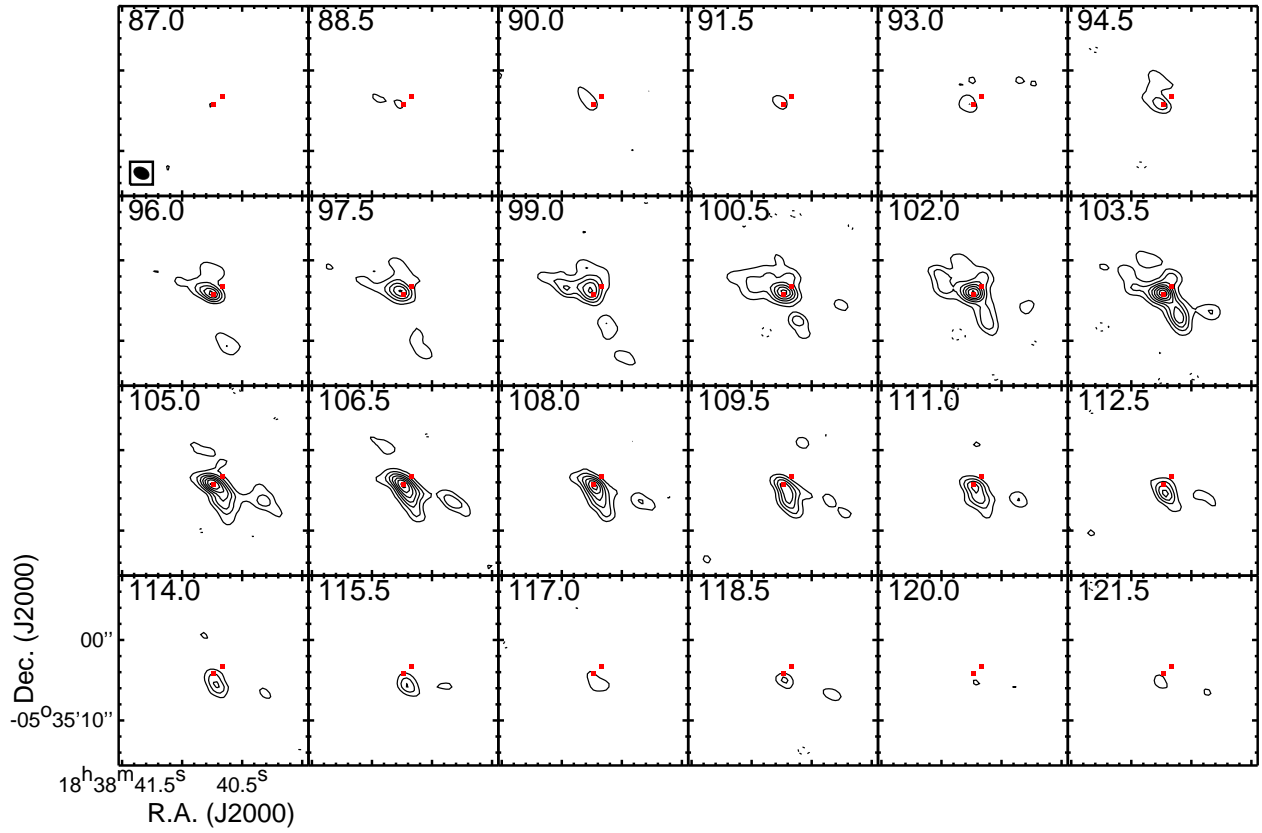


Fig. 5.— SMA SiO (5–4) velocity channel maps. Solid and dotted contours show the positive and negative emission, respectively, with the same absolute levels starting from and increasing in steps of $0.12 \text{ Jy beam}^{-1}$.

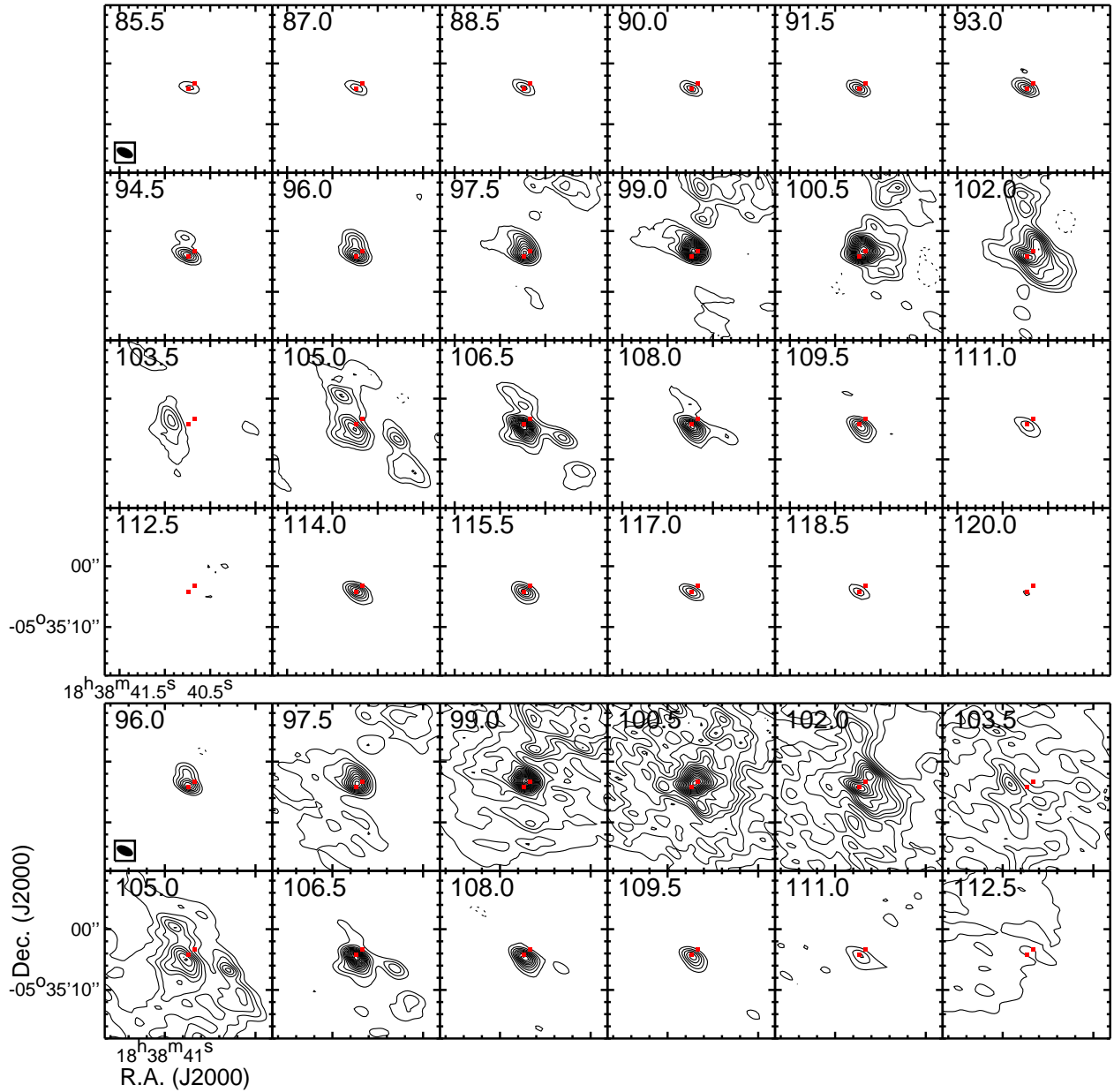


Fig. 6.— SMA ^{13}CO (2–1) velocity channel maps. For channels of 96–112.5 km s^{-1} , the maps made with the combined SMA and IRAM 30m data are shown on the bottom. The contour levels start from and increase in steps of 0.3 Jy beam^{-1} .

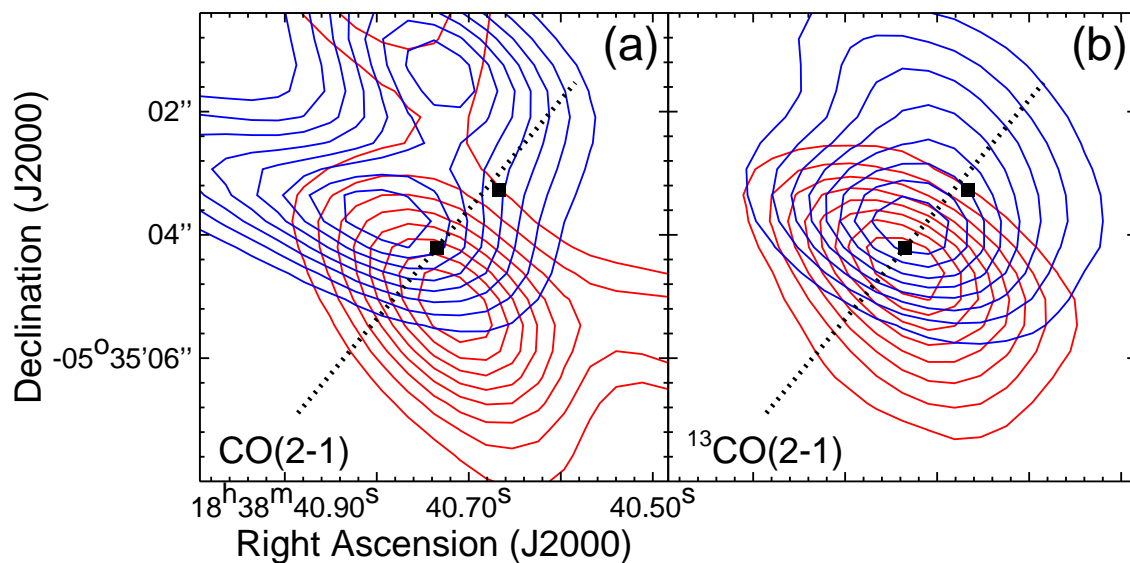


Fig. 7.— (a) A close-up of the SMA CO (2–1) velocity integrated map. Blue and red contours show emission integrated from 69 to 100.5 km s^{−1} and from 106.5 to 139.5 km s^{−1}, respectively. The contour levels start from 20% and increase in steps of 10% of the peak emission, which is 59.1 and 71.3 Jy beam^{−1} km s^{−1} for the blue and red lobes, respectively. (b) The same as (a), but for ^{13}CO (2–1), showing emission integrated from 85 to 102 km s^{−1} and from 105 to 120 km s^{−1}. The peak emission is 37.7 and 26.2 Jy beam^{−1} km s^{−1} for the blue and red lobes, respectively.

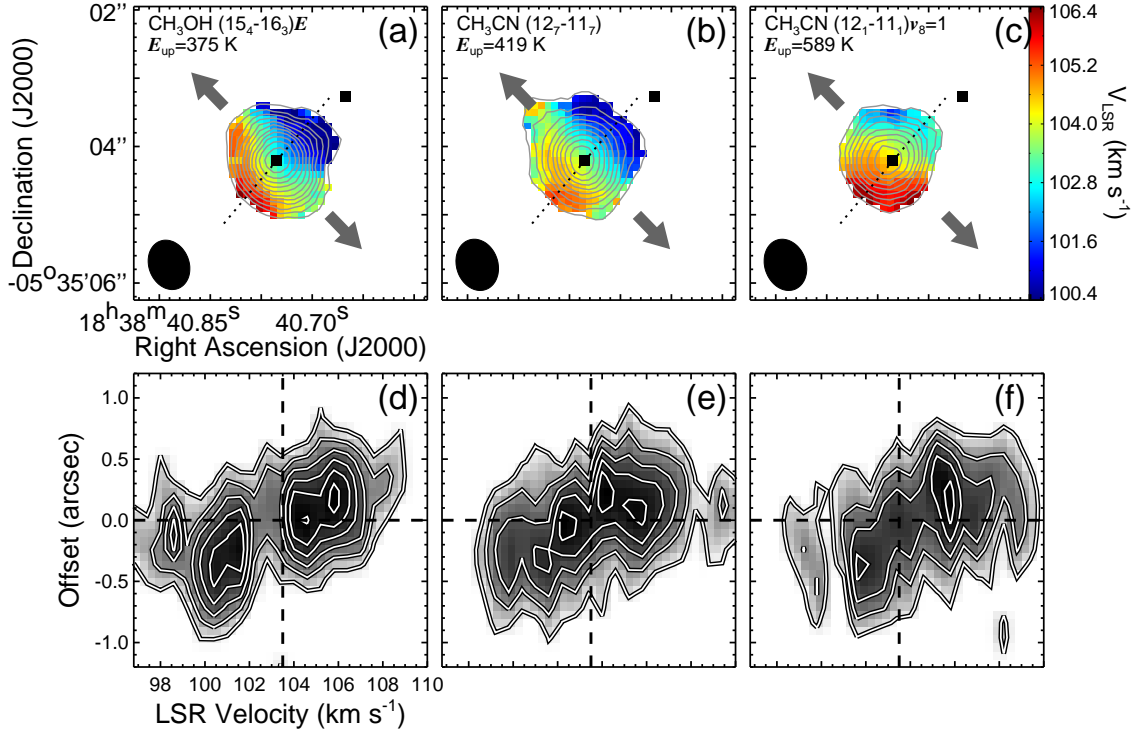


Fig. 8.— (a): The color image shows the first moment map of the CH₃OH (15_{4,11}-16_{3,13})E emission. The gray contours show the zeroth moment map starting from 1.0 Jy km s⁻¹ and increasing in steps of 0.8 Jy km s⁻¹. A dotted line marks the *P-V* cut at PA=140°. Two arrows are the same as those in Figure 3, indicating the outflow orientation. (b)–(c) Same as (a), but for CH₃CN (12₇-11₇) and vibrational CH₃CN (12₁-11₁). The contour levels in panel (b) start from 0.6 Jy km s⁻¹ and increase in steps of 0.8 Jy km s⁻¹, and in panel (c) start from 1.3 Jy km s⁻¹ and increase in steps of 0.7 Jy km s⁻¹. The color wedge on the right of panel (c) indicates the velocity scale of the first moment maps. (d)–(f) *P-V* diagrams shown in both gray scale and contours. The contour levels all start from 0.21 Jy beam⁻¹, and increase in steps of 0.35, 0.21, and 0.28 Jy beam⁻¹ for CH₃OH (15_{4,11}-16_{3,13})E (d), CH₃CN (12₇-11₇) (e), and vibrational CH₃CN (12₁-11₁) (f), respectively. The horizontal line marks the peak position of MM1, which is taken to be the zero offset. The vertical line denotes the systemic velocity.

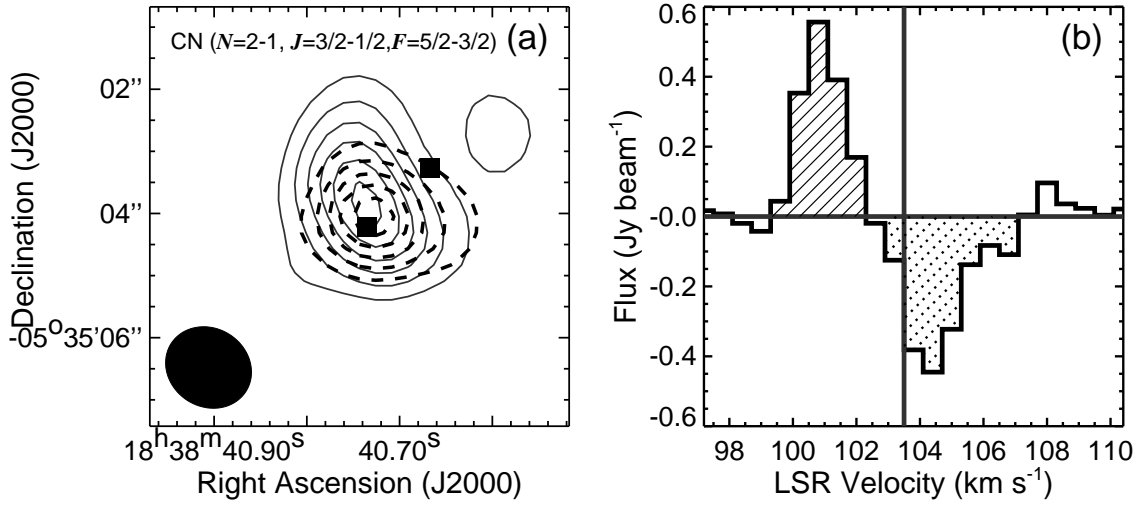


Fig. 9.— (a) Solid and dashed contours show the emission integrated from 96.6 to 102.0 km s⁻¹ and the absorption integrated from 103.2 to 106.8 km s⁻¹, respectively, in CN ($N=2-1$, $J=3/2-1/2$, $F=5/2-3/2$). The starting and spacing contour levels are 54 mJy km s⁻¹ for the emission and -63 mJy km s⁻¹ for the absorption. (b) The spectrum of the same CN transition, extracted from MM1. A vertical line marks the systemic velocity. The velocity channels integrated to show the emission and absorption in (a) are shaded with slashes and dots, respectively.

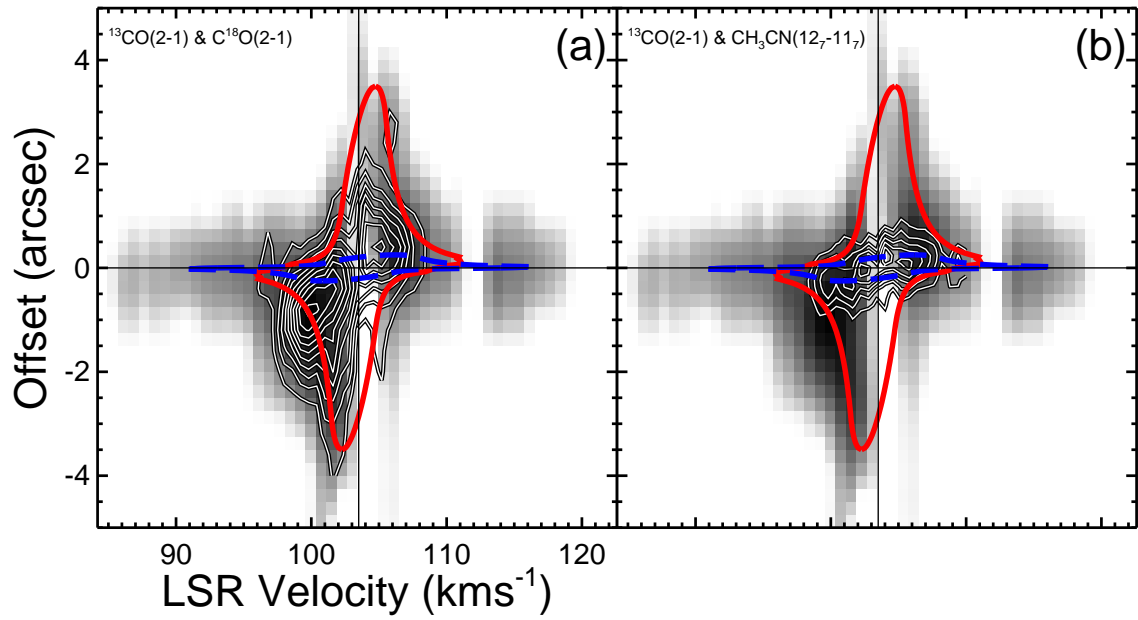


Fig. 10.— The ¹³CO (2–1) *P-V* diagram in gray scale, overlaid with those in C¹⁸O (2–1) (a) and CH₃CN (12₇-11₇) (b) in contours. The C¹⁸O starting and spacing contour levels are 0.21 Jy beam⁻¹. In each panel, the red solid curve shows the model of a free-falling and Keplerian-like rotating envelope, and the blue dashed curve represents the same model but with scaled down parameters (see Section 4.2 for more details of the models).

Table 1. Summary of SMA Observations

Obs. Date (1)	Array Conf. (2)	Freq. Cove. (GHz)		Spec. Res. (kHz) (5)	Bandpass Cal. (6)	Gain Cal. (7)	Flux Cal. (8)	$\tau_{225\text{GHz}}$ (9)
		LSB (3)	USB (4)					
2007 May 17	VEX (6)	219.3 – 221.3	229.3 – 231.3	406.25	3C273	J1743-038, J1911-201	Vesta	0.1
2007 Jul. 08	Comp. (8)	219.3 – 221.3	229.3 – 231.3	406.25	3C273	J1743-038, J1911-201	Vesta	0.07
2008 May 21	Comp. (8)	215.4 – 217.4	225.4 – 227.4	812.5	3C273	J1743-038, J1911-201	Callisto	0.15
2008 Jul. 19	EXT (6)	215.4 – 217.4	225.4 – 227.4	406.25	3C273, 3C454.3	J1743-038, J1911-201	Uranus	0.07

Note. — Col.(1): Observing dates. Col.(2): Array configurations, with the Very Extended, Compact, and Extended configurations abbreviated to VEX, Comp., and EXT, respectively; the figure in parentheses denotes the number of antennas used for each observation. Col.(3)–(4): Approximate ranges of rest frequencies covered in the lower sideband (LSB) and upper sideband (USB). Col.(5): Spectral resolutions. Col.(6)–(8): Bandpass, time dependent gain, and absolute flux calibrators. Col.(9): The averaged 225 GHz opacity.